Low-profile dual-polarized differential-fed filtering antenna and its novel array with low sidelobe level

Quanwei Wu, Yan Shi *, Long Li

School of Electronic Engineering, Xidian University, Xi'an 710071, Shaanxi, China

ABSTRACT

This paper presents a single-layer dual-polarized filtering antenna with good out-of-band suppression. By using inherent characteristic of the patch's eigenmode and meanwhile merging four filtering strategies, i.e., parasitic patches, slot on the driving patch, and defected ground structure (DGS), a low-profile filtering antenna design with five radiation nulls has been realized. With the designed filtering antenna, a conventional 1×2 array with a spacing of 0.91λ is first developed. In order to reduce the sidelobe level of the array, a sharing patching scheme is introduced to decrease the interspace between the elements as 0.44λ, with the same physical size as the conventional array. In addition, a concept to measure total isolation between two kinds of the polarized ports in the array, i.e., S_{ddVH}, has been derived for the first time. The prototype of the proposed array is fabricated with a profile of 0.038λ. Measured results indicate that the designed novel array has an operational band of 3.53–4.06 GHz, S_{ddVH} better than 41 dB, a sidelobe level below -18 dB, and a suppression level above 20 dB with the stopband up to 0.5 GHz and 5 GHz.

© 2023 Karabuk University. Publishing services by Elsevier B.V. This is an open access article under the CC BY-NC-ND license (http://creativecommons.org/licenses/by-nc-nd/4.0/).

1. Introduction

With the rapid development of the fifth-generation (5G) mobile communication system and space-borne synthetic aperture radar (SAR) system, more and more communication frequency bands and standards have been put forward, inevitably leading to electromagnetic interference and crosstalk. Therefore, as shown in Fig. 1, it is necessary for the transceiver system to have an ability to filter out the interference. Wireless communication system and space-borne SAR system have the trend of miniaturization and integration, which imposes higher requirements on the sizes of the RF front-ends including filter, antenna, and its array.

The integration of antenna and filter is called filtering antenna, which can effectively reduce the volume and the loss of the RF front-end. The design methods of the filtering antenna can be divided into two categories. The first one is a filtering antenna with a filter as the main body. By cascading the antenna after the filter [1,2] or replacing the last stage of the filter with an antenna [3–6], the filtering characteristics are achieved to some extent. Thus, the focus of the design is biased toward the radiation performance [7,8], such as bandwidth, gain, and polarization, etc. The second kind of the filtering antennas is based on the antenna [9–22], by introducing specific structures into the feeding structure and radi-

ators of the antenna, for instance slot [10,14], parasitic patch [11,15], defected ground structure (DGS) [18,21], and so on, to achieve the frequency selectivity responses. Its design emphasis is on the frequency selectivity characteristics [17–24], including out-of-band suppression, steep roll-off, stopband width, etc. The latter design method has a higher integration than the former. However, it can be found from the published designs that when the dual-polarized filtering antenna by using the slot, parasitic patch, and DGS is designed, the multilayer structure is often employed, thus giving rise to high antenna profile.

With the filtering antenna element, design of the filtering antenna array has been a hot topic. In [13], a 1-by-3 dual-polarized filtering antenna array with an inter-element spacing of 0.5λ for the base station application was designed, and meanwhile two 1-to-3 power dividers are used to feed the array. The isolation between the input ports of two power dividers used to measure polarization isolation is 17 dB, and the sidelobe level of the array is 12 dB. In [20], two 1-by-6 antenna arrays fed by two 1-to-6 power dividers, respectively, was proposed to operate in DCS and WCDMA bands. By measuring the input ports of two power dividers, the isolation of two frequency bands is 35 dB. And the sidelobe level is 16 dB with the antenna spacing of 0.78λ in the DCS band/0.89λ in the WCDMA band. In [17], a 4-by-4 dual-polarized array with a compact size of $3.13\lambda \times 3.13\lambda \times 0.16\lambda$ fed by two power dividers is designed. The polarization isolation between the input ports of two power divi-
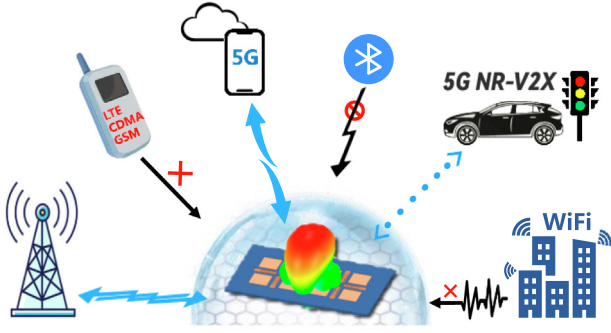
Fig. 1. Application scenario and function diagram of filtering antenna for 5G.

ders is 30 dB. However, in order to reduce the mutual coupling, an extra isolation wall was introduced, thus increasing design complexities. Therefore, it can be found from the reported references that the isolation of the array is measured after the array is connected to the power divider. The resultant isolation depends on not only antenna array itself but also the power divider. In addition, how to obtain both high polarization isolation and low sidelobe is still a challenging problem in the filtering antenna array design.

In this paper, a dual-polarized filtering antenna consisting of driven patches and radiation patches and its novel low-profile array with both high polarization isolation and low sidelobe level have been proposed. The contribution of the paper has two folds. One is to fuses several filtering methods including inherent eigenmode, parasitic patches, slot, and defected ground structure (DGS) to achieve good filtering performance without increase of the antenna profile. The second is to develop a dual-polarized filtering antenna array with both high polarization isolation and low sidelobe performance. The designed filtering antenna fabricated on a single-layer substrate, and with five radiation nulls, the resultant stopband covers GSM, CDMA and LTE bands. Based on the symmetry of the antenna structure, the interspace between the antenna elements can be reduced from 0.91λ to 0.44λ by sharing the radiating patches, and thus sidelobe level of the proposed array decreases from -12.36 dB to -18.11 dB. In addition, the polarization isolation of the array itself without the consideration of the power divider, i.e., the total isolation between two kinds of the polarized ports in the array named S_{ddVH} and S_{ddHV}, are proposed for the first time. The designed array has high polarization port isolation above 41.1 dB. Good agreement between the simulation and the measurement verifies the proposed design.

2. Filtering antenna design

Various filtering antennas have been developed hitherto. Among these filtering antenna designs, a large number of dual-polarized filtering antennas have been studied, but most of them are multilayer structures, with the higher profiles [2,5,13,14,20]. In addition, a number of single-layer filtering antennas with single polarization have been proposed [10,16,19]. Here, an integrated design of a single-layer low-profile dual-polarization filtering antenna is proposed. This section includes the antenna configuration, the design process of the proposed antenna, and performance comparison between the simulated and measured results.

2.1. Filtering antenna configuration

Fig. 2 shows the proposed filtering antenna, which consists of one single layer copper-coated substrate with relative permittivity of 2.65 and loss tangent of 0.001. Two pairs of chamfered driven
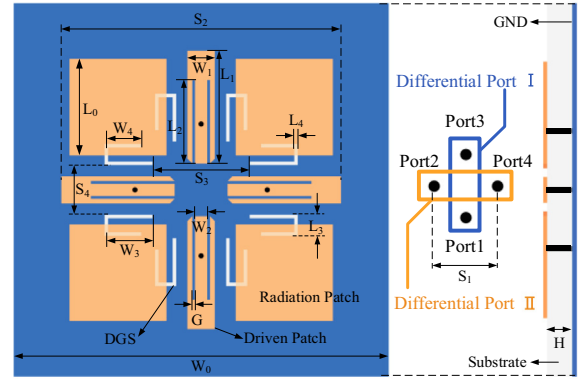

Fig. 2. Configuration of the proposed filtering antenna (unit: mm): $W_0 = 100$, $W_1 = 6.2$, $W_2 = 2.9$, $W_3 = 10.5$, $W_4 = 7.9$, $L_0 = 20.9$, $L_1 = 25.7$, $L_2 = 19$, $L_3 = 4.2$, $L_4 = 0.7$, $S_1 = 28.4$, $S_2 = 61.8$, $S_3 = 18$, $S_4 = 9.1$, $G = 0.5$, $H = 3$.

patches and four square radiation patches evenly distributed around them are fabricated on the top surface of the substrate. Four pairs of slots are etched on four driven patches, and four pairs of Γ-shaped slots are etched on the ground to improve low-frequency and high-frequency selectivities, respectively. Two kinds of polarized waves are excited by two pairs of the differential probes connected to the driven patches. Here, the differential port I consisting of ports 1 and 3 excites x-polarization wave and the differential port II composed of ports 2 and 4 excites y-polarization wave.

2.2. Operating mechanism of filtering antenna

To clearly demonstrate the design idea and working mechanism of the proposed antenna, the design process of the antenna is shown in Fig. 3. Antenna I consists of two pairs of the chamfered rectangular patches which are placed along x and y axes, respectively, and are fed by two pairs of differential ports. Antenna II adds four square radiation patches placed around the driven patches. Antenna III is formed by introducing a pair of slots on each driven patch. And then, four pairs of Γ-shaped DGSs are introduced on the ground around the probes to form the antenna IV, i.e., the proposed antenna.

Fig. 4 gives the simulated differential S-parameter $|S_{dd11}|$ and broadside gains of the antennas I $\sim$ IV. Here, we only discuss the case of x-polarization. Due to the symmetry of the antenna structure, the same conclusions hold for the y-polarization. For a typical four-port network including two pairs of the differential ports, the widely used differential S-parameters can be written as

$$\begin{cases} S_{dd11} = (S_{11} - S_{31} - S_{13} + S_{33})/2 \\ S_{dd22} = (S_{22} - S_{42} - S_{24} + S_{44})/2 \\ S_{dd12} = (S_{12} - S_{32} - S_{14} + S_{34})/2 \\ S_{dd21} = (S_{21} - S_{41} - S_{23} + S_{43})/2 \end{cases} \quad (1)$$
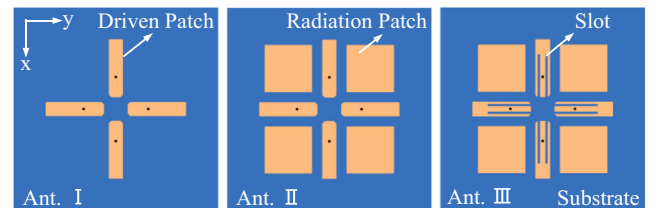

Fig. 3. The design procedure from antenna I to antenna II to antenna III. The geometric dimensions of each antenna (unit: mm): $L_1 = 26.7$, $S_1 = 32.4$, $S_2 = 63.8$ for antenna I; $L_0 = 21$, $L_1 = 27.6$, $S_1 = 27.6$, $S_2 = 63.6$ for antenna II; $L_0 = 21$, $L_1 = 25.9$, $S_1 = 27$, $S_2 = 60.2$ for antenna III.
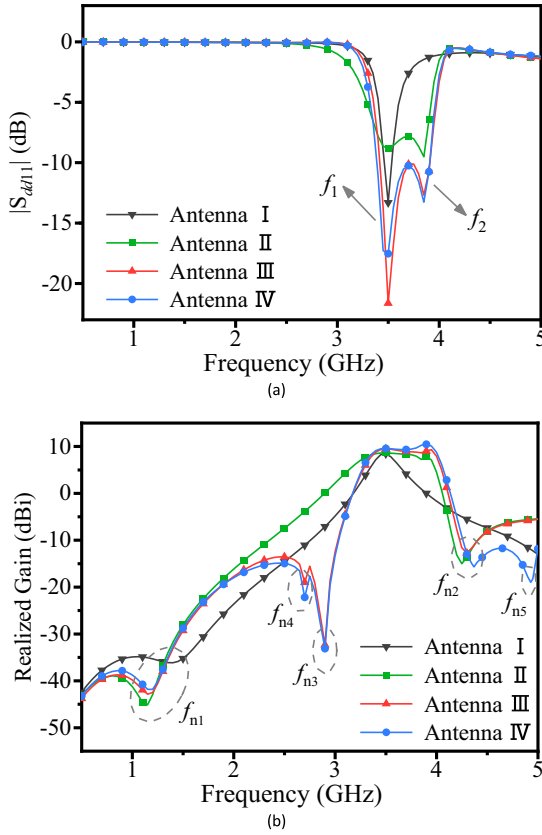
Fig. 4. The $|S_{dd11}|$ and realized gain of antennas I, II, III, IV. (a) $|S_{dd11}|$. (b) Realized gain.

2.2.1. Analysis of resonance and radiation null of antenna I

As shown in Fig. 4, antenna I has a resonance at f_1 = 3.5 GHz and a radiation null at f_{n1} = 1.4 GHz. Fig. 5 gives the surface current distributions of the antenna I at f_1 and f_{n1}. At f_1, the surface current on each of two driven patches along x-axis is maximal in the middle and zero at the two ends, and therefore the resonant mode is TM$_{10}$ mode. The corresponding length of each driven patch is a quarter wavelength at f_1. On the other hand, it can be observed from the surface current distribution at f_{n1} that the currents on the both sides of the feeding location flow in an opposite direction, resulting in radiation cancellation in broadside direction. In order to better explore the inherent radiation null, the eigenmodes of the antenna I are solved. The electric field distributions of the eigenmode 3 at the resonant frequency f_{mode3} = 1.435 GHz are given in Fig. 6. For comparison, the electric field distributions of the antenna I at f_{n1} = 1.4 GHz are given. Considering that the driven patch consists of four same rectangular patches, the eigenmode 3 has four same electric fields distributing on the four patches,
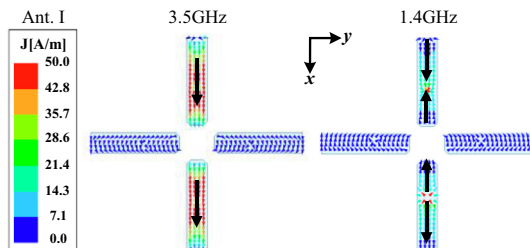
respectively, as shown in Fig. 6(a). When two patches along x axis are excited by the differential signals, i.e., two signals with the equal magnitude and 180° out of phase, the opposite electric field distributions of the eigenmode 3 on the two patches along x axis are obtained, as shown in Fig. 6(b). On the other hand, without the excitations for two patches along y axis, there are no electric fields of the eigenmode 3 on the two patches along y axis. In addition, the similar operating frequencies for the eigenmode 3 and the radiation null are observed. Therefore, the radiation null at f_{n1} is an inherent radiation null corresponding to the eigenmode 3.

2.2.2. Analysis of resonance and radiation null of antenna II

When the radiation patches are placed around the driven patch (antenna II), a new resonance at f_2 = 3.85 GHz is excited and thus the working bandwidth is widened, as shown in Fig. 4. Meanwhile, a radiation null at f_{n2} = 4.25 GHz is generated to improve the high-frequency roll-off. Fig. 7 shows the surface current distributions of antenna II at f_1, f_2, and f_{n2}. It can be seen that the driven patch is still in resonance at f_1 = 3.5 GHz, and the radiation patch resonates at f_2 = 3.85 GHz. Besides, at f_2 the currents on the four radiation patches are superimposed on each other in the x direction and cancelled out in the y direction, thus achieving the x-polarization radiation. The opposite current distributions on the radiation patches and the driven patches are due to the capacitive coupling between them. However, the currents flowing on the driven patches are far weaker than those on the radiation patches. It means that the energy is well coupled from the driven patches to the radiation patches. Therefore, good radiation is generated by the radiation patches at 3.85 GHz. At f_{n2} = 4.25 GHz, the weak currents on the radiation patches are observed, compared with those at f_2. As shown in Fig. 8, an equivalent model for the coupling between the driven and radiation patch is built to investigate the operating mechanism of the radiation null at f_{n2}. With the symmetry of the antenna, only a quarter of the whole antenna structure, i.e., a driven patch and a radiation patch, is analyzed. The driven and radiation patches are close together, and thus can be equivalent to two parallel coupling lines with four ports, i.e., ports (i), (ii), (iii) and (iv). It is worthwhile pointing out that the four ports different from the actual feeding ports are used to analyze the coupling effect in the parallel coupling lines. According to the even and odd analysis of the parallel coupling line in [25], when the port (i) is driven by an input voltage of 2 V_0, the voltages of the ports (ii), (iii) and (iv), i.e., V_2, V_3 and V_4, can be solved, respectively, as

$$V_2 = V_0 \frac{\sqrt{1-C^2}}{\sqrt{1-C^2}\cos\theta + j\sin\theta} \qquad (2)$$

$$V_3 = V_0 \frac{jC\tan[03B8]}{\sqrt{1-C^2} + j\tan\theta} \qquad (3)$$

$$V_4 = 0 \qquad (4)$$

Fig. 5. Surface current distributions on the driven patch of the antenna I at 3.5 GHz and 1.4 GHz.
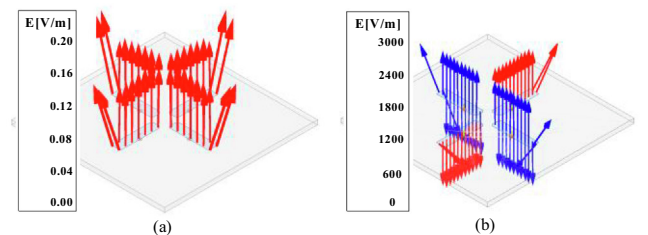

Fig. 6. Electric field distributions on the driven patch of the antenna I. (a) Model electric field at f_{mode3}. (b) Surface electric field at f_{n1}.
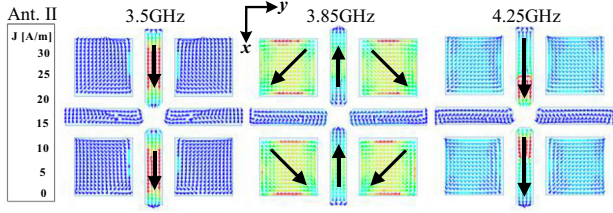
Fig. 7. Surface current distributions on the driven patches and radiation patches of the antenna II at f_1 = 3.5 GHz, f_2 = 3.85 GHz, and f_{n2} = 4.25 GHz.
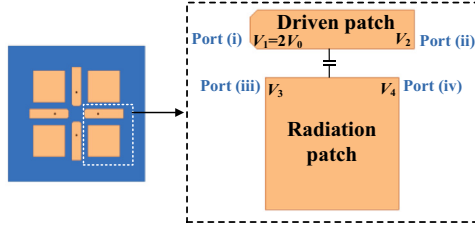

Fig. 8. The equivalent circuit model of parallel coupled lines composed of a driven patch and a radiation patch.

where C is voltage coupling coefficient, θ is the electric length of the radiation patch. Fig. 9 shows the variations of V_2 and V_3 with the θ. It can be seen that when $\theta = n\pi$ (n = 0,1, ...), the V_3 is zero, meaning that electromagnetic energy cannot be coupled from the driven patch to the radiation patch.

When $\theta = \pi$, the length of the radiation patch is equal to half of the wavelength at f_{n2}. In this scenario, the radiation null is formed, and the corresponding frequency f_{n2} is obtained as

$$f_{n2} = \frac{c}{2(L_0 + 2\Delta L)\sqrt{\varepsilon_{eff}}} \quad (5)$$

where c represents the speed of light, L_0 represents the length of the radiation patch, ΔL represents the fringing length extension, and ε_{eff} represents the effective relative permittivity. With (5), the theoretical estimation of the f_{n2} is given as 4.2 GHz, approximately equal to the full-wave simulation results of 4.25 GHz.

2.2.3. Analysis of resonance and radiation nulls of antenna III

A pair of the slots is etched on each driven patch to form the antenna III. As shown in Fig. 4(b), the use of the slot is to introduce two adjacent radiation nulls at f_{n3} = 2.9 GHz and f_{n4} = 2.7 GHz for improvement of the low-frequency roll-off. Fig. 10 gives the surface current distributions of the antenna III at f_{n3} and f_{n4}. At f_{n3} = 2.9-GHz, the currents mainly distribute near the slots of the excited driven patches along x direction. By contrast, the currents at f_{n4} = 2.7 GHz distribute near the slots of the driven patches along both x and y directions. Compared to the currents at f_{n3}, the currents at f_{n4} flow in a longer path, and thus the f_{n4} is lower than
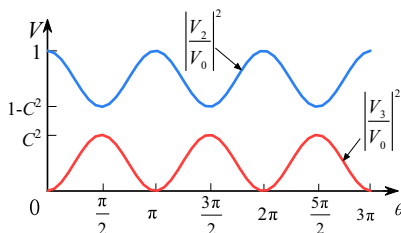

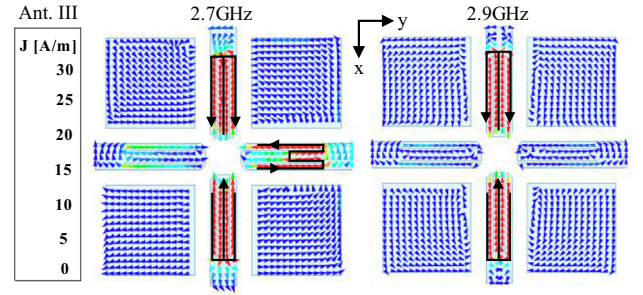**Fig. 9.** Variation of the port voltage with the coupling line length.

Fig. 10. Surface current distributions of antenna III at f_{n4} = 2.7 GHz and f_{n3} = 2.9 GHz.

the f_{n3}. In addition, there is a small convex of the gain curve between f_{n3} and f_{n4}, as shown in the Fig. 11. That is due to the coupling between the driving patch along x direction and the driving patch along y direction which are too close together. The coupling between the driving patches can be reduced by corner-cutting to avoid sharp convex.

In order to analyze the two radiation nulls, an equivalent circuit is established, as shown in Fig. 12. Each of the driven patches appears as a shunt RLC circuit consisting of the inductor L_d, the capacitor C_d and the resistor R_d with the band-pass response. A pair of the slots is regarded as a shunt LC circuit composed of the inductor L_s, the capacitor C_s with the band-stop characteristic, which is connected to the RLC circuit in series. At the resonant frequency of the band-pass circuit, the impedance of the RLC circuit is the R_d, thus achieving the radiation of the driven patch. On the other hand, at the resonant frequency of the band-stop circuit, the impedance of the LC circuit becomes infinite. Therefore, the energy cannot be transmitted from the feeding port to the radiation resistor R_d but is concentrated around the slot, thus generating the radiation null. At f_{n3} = 2.9 GHz, the length of the slot L_2 is a quarter of the wavelength at the resonant frequency of the LC circuit. As a result, the relationship between the f_{n3} and the L_2 is

$$f_{n3} = \frac{1}{2\pi\sqrt{L_s C_s}} = \frac{c}{4(L_2 + \Delta L)\sqrt{\varepsilon_{eff}}} \quad (6)$$

In addition to the radiation null at f_{n3} = 2.9 GHz, there is a radiation null at f_{n4} = 2.7 GHz, which can be still analyzed according to the equivalent circuit model shown in Fig. 12. The only difference between two radiation nulls is a coupling between the excited driven patches along x direction and the unexcited driven patches along y direction at f_{n4}. Therefore, the electromagnetic energy excited by the feeding probe distributes on the slots along both x and y directions.
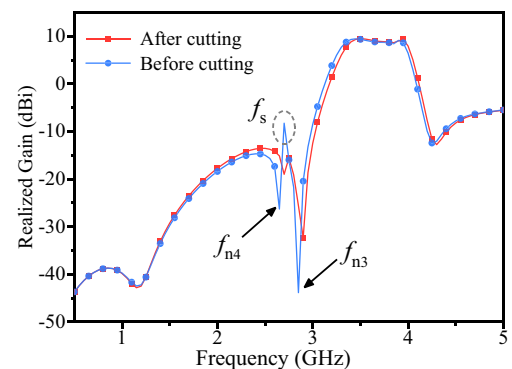

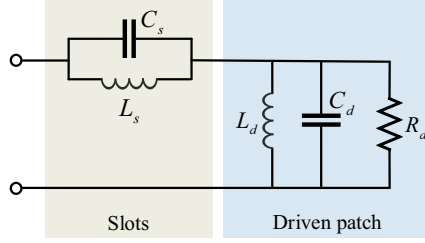**Fig. 11.** Influence of driven patches without and with corner-cutting on realized gain curve.

Fig. 12. The equivalent circuit of the driven patch and slots.

Fig. 14. (a) The electric field and (b) the current distributions on GND of antenna IV at f_{n5} = 4.95 GHz.

2.2.4. Analysis of resonance and radiation null of antenna IV

The antenna IV, i.e., the proposed antenna, is achieved by etching a pair of the DGSs around each probe on the ground. According to Fig. 4(b), an extra radiation null at f_{n5} = 4.95 GHz is generated to extend the high-frequency stopband. The operating mechanism of the DGS for the radiation null can be explained in terms of the equivalent circuit, as shown in Fig. 13. The DGS is regarded as a parallel LC circuit with a bandstop response including the inductor L_g and the capacitor C_g [26], which is cascaded before the equivalent circuit shown in Fig. 12. Similar to the slots on the driven patches, at the resonant frequency of the LC circuit of the DGS, i.e., f_{n5}, the corresponding impedance is infinite, thus binding the energy around the DGS to achieve a radiation null, as shown in Fig. 14. The overall length of the DGS is $2*(L_3 + W_3 + W_4)$, which equals a wavelength at f_{n5}. Thus, the f_{n5} can be given as

$$f_{n5} = \frac{1}{2\pi\sqrt{L_g C_g}} = \frac{c}{2(L_3 + W_3 + W_4)\sqrt{\varepsilon_{eff}}} \tag{7}$$

It is worthwhile noticing that the equivalent circuit for the DGS shown in Fig. 13 is established without the considerations of the radiation patches.

As shown in Fig. 15, the antenna IV operates in a band of 3.39–3.91 GHz with an in-band gain about 10 dBi. Five radiation nulls achieve a wide out-of-band suppression, i.e., above 25.4 dB at low-frequency band greater than 0.5 GHz and above 22.2 dB at high-frequency band up to 5 GHz.

The obtained radiation nulls in the process of the antenna design can be controlled independently. Fig. 16(a) shows the inherent radiation null at f_{n1} can be adjusted in terms of the feeding position S_1. As S_1 increases, the inherent null shifts toward higher frequencies. Fig. 16(b) depicts variation of the radiation null at f_{n2} with the L_0. As the L_0 decreases, the f_{n2} shifts toward the higher frequencies with the fixed f_{n1}, as shown in (5). Fig. 16(c) shows that the radiation nulls at f_{n3} and f_{n4} can be controlled by tuning the length of the slot L_2. As L_2 increases from 18 mm to 20 mm, two radiation nulls move toward the lower frequencies simultaneously, whereas other radiation nulls remain unchanged. Fig. 16(d) shows the variation of the f_{n5} with the W_3. The f_{n5} increases with the decrease of W_3.
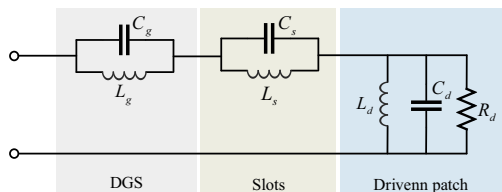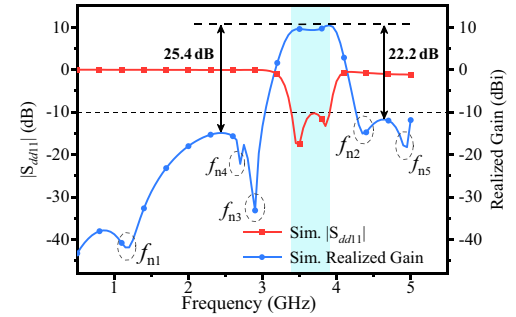

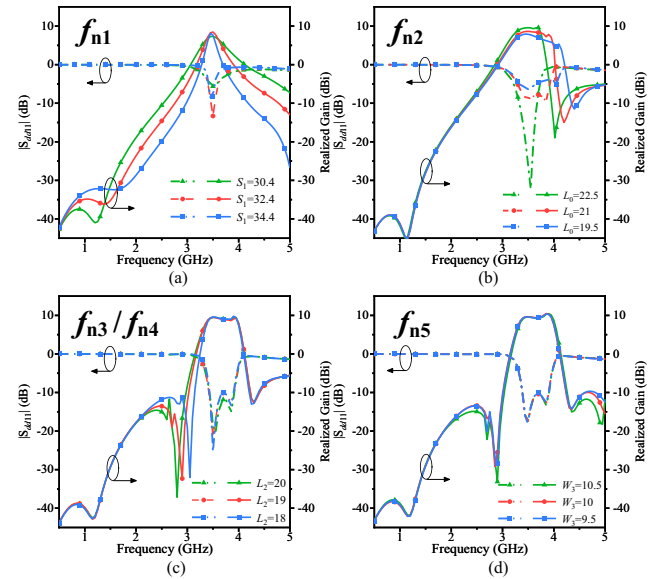**Fig. 15.** Simulated $|S_{dd11}|$ and realized gain of the proposed antenna.

Fig. 16. (a) Variation of the radiation null at f_{n1} with the S_1 in antenna I. (b) Variation of the radiation null at f_{n2} with the L_0 in antenna II. (c) Variation of the radiation nulls at f_{n3} and f_{n4} with the L_2 in antenna III. (d) Variation of the radiation null at f_{n5} with the W_3 in antenna IV.

2.3. Measurement results and discussions

To validate the designed filtering antenna, a prototype is fabricated and measured, as shown in Fig. 17. Here, due to the symmetry of the antenna, only the measurement results for x polarization are given. The simulated and measured results of $|S_{dd11}|$, gain, and $|S_{dd21}|$ are shown in Fig. 18. The simulated operating bandwidth of the proposed antenna ($|S_{dd11}|<-10$ dB) is 3.39–3.91 GHz (14.3%) and the measured bandwidth is 3.53–4.06 GHz (14%). The slight
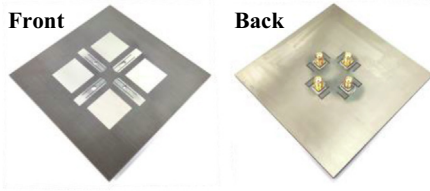

Fig. 13. The equivalent circuit of the DGS and radiation patch.

Fig. 17. Photographs of the proposed filtering antenna.

frequency offset is mainly attribute to fabrication error, SMA soldering error, substrate tolerance, etc. The simulated out-of-band suppression levels are better than 25.4 dB at low-frequency band greater than 0.5 GHz and 22.2 dB at high-frequency band up to 5 GHz, respectively, whereas the measured results are 25.8 dB and 22.1 dB, respectively with the same suppression bandwidths. The five radiation nulls are well observed according to the measured gain curve, and the simulated and measured broadside gains have the same peak value of 10 dBi. The simulated differential port isolation $|S_{dd21}|$ is greater than 46.8 dB in the whole band. By comparison, the measured one is above 41 dB, with the similar variation trend to the simulated result.

Fig. 19 gives the normalized radiation patterns in E-plane and H-plane at 3.5 GHz, 3.65 GHz, and 3.8 GHz, respectively. The simulated and measured cross-polarization ratios are above 51.5 dB and 27 dB, respectively. Here, the discrepancy between them mainly comes from the fabricating and measuring errors. To sum up, an integrated design of a single-layer filtering antenna is verified, and its frequency selectivity and radiation characteristics meet the expectations.

3. Novel filtering antenna array

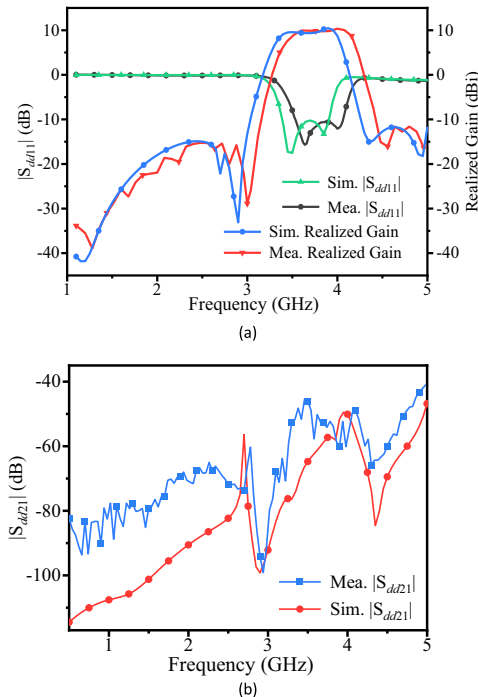With the designed filtering antenna, the filtering antenna array has been developed in this section.

Fig. 18. Simulated and measured $|S_{dd11}|$, realized gain, and $|S_{dd21}|$ of the proposed filtering antenna. (a) $|S_{dd11}|$ and realized gain. (b) $|S_{dd21}|$.
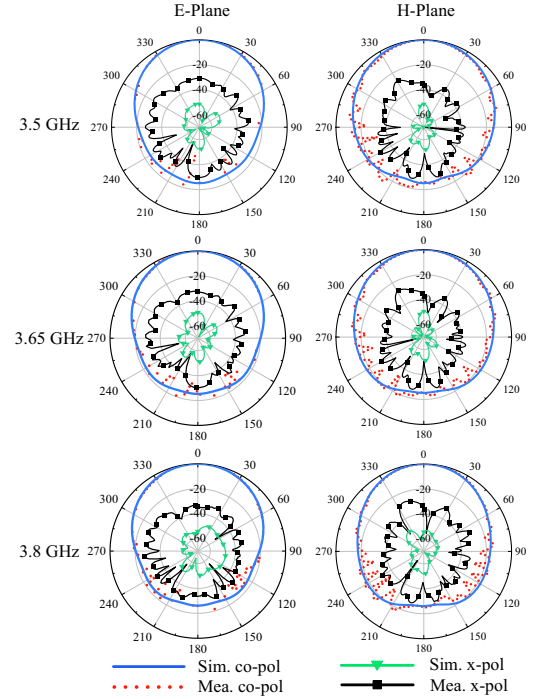

Fig. 19. Simulated and measured normalized radiation patterns of the proposed antenna in E-plane and H-plane at 3.5 GHz, 3.65 GHz, and 3.8 GHz.

3.1. Conventional 1 × 2 array design (array I)

Firstly, a conventional 1 × 2 antenna array is designed based on the proposed filtering antenna element with an element spacing of $D = 0.91\lambda$, which is called array I, as shown in Fig. 20. Here λ is wavelength at the center frequency. As shown in Fig. 21(a), a prototype is fabricated, and comparison of the simulated and measured gains for x and y polarizations is given in Fig. 22. The measured out-of-band suppression levels for x polarization are above 26.1 dB in low-frequency band greater than 0.5 GHz and above 27 dB in high-frequency band up to 5 GHz, respectively, and those for y polarization are 24.1 dB and 26.4 dB in the same bands, respectively.

In order to evaluate and measure the overall polarization isolation performance of the antenna itself, two kinds of the polarization ports in the array are considered. Specifically, all x-polarization ports are denoted as the port V, and all y-polarization ports are denoted as the port H. Thus, S_{ddHV} is the differential S parameter from the port V to the port H, and S_{ddVH} represents the differential S parameter from the port H to the port V, which distinguishes them from widely used polarization isolation of the antenna array with the power divider. The S_{ddHV} and S_{ddVH}
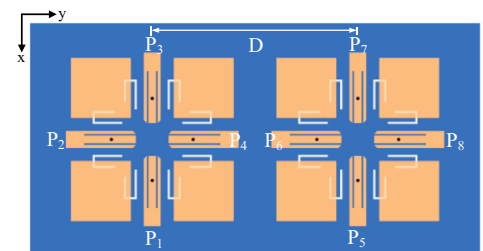

Fig. 20. Layout of the proposed filtering antenna array I and the diagram of port distribution. The geometric dimensions of the array I (unit: mm): $L_0 = 21$, $S_1 = 29$, $L_1 = 24.8$, $D = 72.2$ (0.91λ).
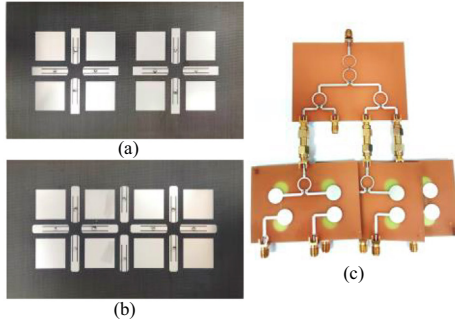
Fig. 21. Photographs of the filtering antenna array and feed network: (a) Array I. (b) Array II. (c) Feeding network.
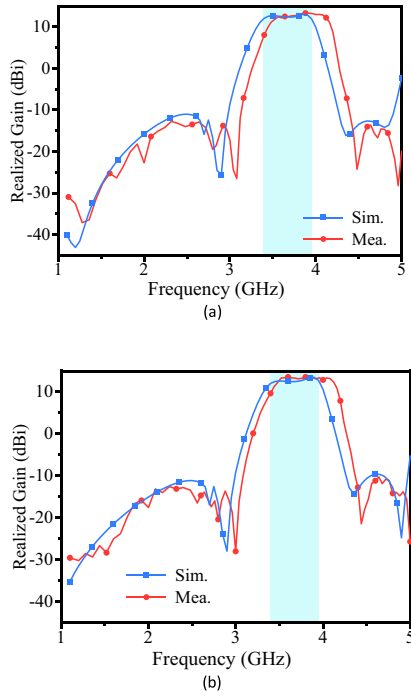

Fig. 22. Simulated and measured realized gains of the array I. (a) *x* polarization. (b) *y* polarization.

Fig. 23. Simulated and measured |S_{ddVH}| of the array I.

Fig. 24. Simulated and measured normalized radiation patterns in E-plane and H-plane of the array I at 3.65 GHz for *x*-polarization feeding ports and *y*-polarization feeding ports.

are defined to measure the polarization purity of the ports to some extent. It is worthwhile pointing out that S_{ddHV} and S_{ddVH} are different from the cross-polarization ratio. The former is the port-related parameter, whereas the latter is radiation-related parameter. As for the array I with the port distribution shown in Fig. 20, S_{ddVH} is given as

$$S_{ddVH} = \frac{1}{4}[(S_{12} - S_{32} + S_{52} - S_{72}) - (S_{14} - S_{34} + S_{54} - S_{74}) \\ + (S_{16} - S_{36} + S_{56} - S_{76}) - (S_{18} - S_{38} + S_{58} - S_{78})] \qquad (8)$$

The derivation details of Eq. (8) can be found in the Appendix. As shown in Fig. 23, the simulated and measured S_{ddVH} are higher than 58.1 dB and 39.8 dB in the entire frequency band, respectively. Fig. 24 gives the simulated and measured normalized radiation patterns in E-plane and H-plane at 3.65 GHz, in good agreement, with the simulated and measured sidelobe levels of −10.9 dB and −12.36 dB, respectively. The simulated and measured cross-polarization ratios are above 48.4 dB and 27 dB, respectively.

In order to measure the in-band radiation and out-of-band suppression characteristics, an ultra-wideband phase-shift power splitter is designed to provide the desirable signals of the array I.
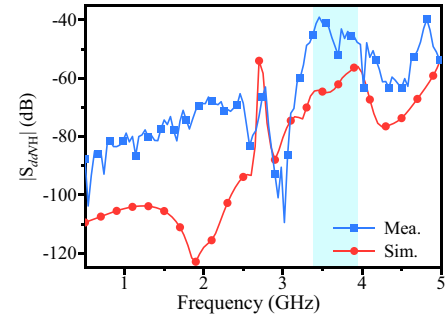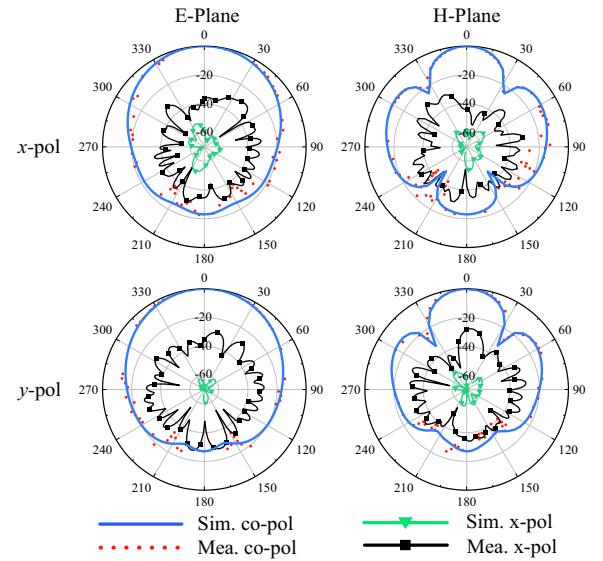
As shown in Fig. 21(c), the feed network is composed of a 1-to-2 Wilkinson power divider and several power dividers with two ±90° output phase shifts. Here, microstrip-slotline-microstrip transition is used to achieve the desirable phase shift. Due to different directions of the coupling from the slotline to the microstrip, two output signals of equal amplitude with a difference of ±90° are generated within the ultra-wideband. The measurement results of the phase shifter are shown in the Fig. 25. The operating band (|S_{11}|<−10 dB) covers 1.1 GHz to 5 GHz. The |S_{21}|, which represents the insertion loss of the phase shifter, is about 5 dB, and a nearly perfect 180° phase difference is obtained.
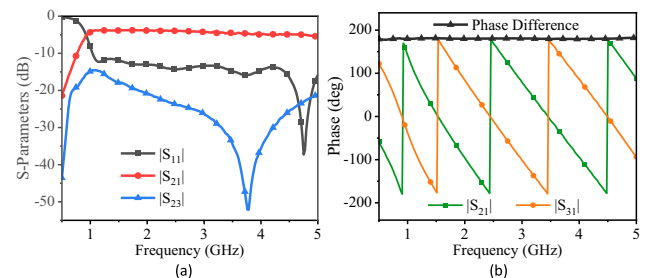

Fig. 25. The measured result of (a) S parameter of phase shifter and (b) the phase difference between the two output ports.

3.2. Improved array design (array II)

Owing to the conventional array arrangement, the sidelobe level of the above 1 × 2 array is high. In order to reduce the side-lobe level, the driven patches and radiation patches can be reused to decrease the interspace between the elements. Specifically, one driven patch and two radiation patches are shared between two adjacent elements, and the resulting filtering array is called array II, as shown in Fig. 26. The improved array has the same physical size as the conventional 1 × 2 array, and the corresponding element spacing is reduced from $D = 0.91\lambda$ to $D = 0.44\lambda$. It should be noted that to better share the adjacent patches, all corners on the driven patches are cut off. Besides, it can be noticed that the elements 1 and 2 at two sides of the array are exactly same, different from the element 3 in the middle of the array. Specifically, the orientations of the slots on driven patches and the DGS and the feed position of the element 3 are opposite to those of the elements 1 and 2. But the difference between them has no effect on the overall performance of the array II. In order to achieve the differential feeding for all elements, the used feeding scheme is shown in Fig. 27.

The array II is also fabricated and shown in Fig. 21(b). The simulated and measured gains are shown in Fig. 28, in good agreement. For comparison, the simulated and measured results of the array I are also given. Similar gains are obtained by the arrays I and II. The measured out-of-band suppression levels for *x* polarization are above 22.1 dB in low-frequency band greater than 0.5 GHz and above 19.7 dB in high-frequency band up to 5 GHz, respectively, and those for *y* polarization in the same bands are 24.8 dB and 23.8 dB, respectively. As shown in Fig. 29, the simulated and measured $|S_{ddVH}|$ are 47 dB and 41.1 dB, respectively, meaning that the array II has better polarization isolation performance. Here, the S_{ddVH} of the array II is solved as

$$S_{ddVH} = \frac{1}{4}[(S_{12} - S_{32} + S_{52} - S_{72} - S_{92} + S_{10\_2})$$
$$- (S_{14} - S_{34} + S_{54} - S_{74} - S_{94} + S_{10\_4})$$
$$+ (S_{16} - S_{36} + S_{56} - S_{76} - S_{96} + S_{10\_6})$$
$$- (S_{18} - S_{38} + S_{58} - S_{78} - S_{98} + S_{10\_8})] \tag{9}$$

Derivations about the S_{ddVH} can be found in the Appendix.

Besides, Fig. 30 shows the simulated and measured normalized patterns of the array II at 3.65 GHz. The simulated and measured sidelobe levels are −20 dB and −18.11 dB, respectively, and the simulated and measured cross-polarization ratios are above 46 dB and 26 dB, respectively. As shown in Fig. 31, compared to the array I with the same physical size, the simulated and measured sidelobe levels of the array II decrease by 9.1 dB and 6 dB, respectively. It is worthwhile pointing out that the proposed sharing patch method can be easily extended to $m \times n$ array by adding $(m\text{-}1) \times (n\text{-}1)$ elements.
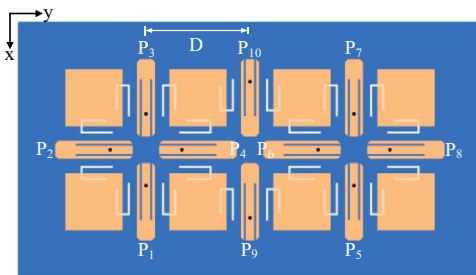

Fig. 26. Layout of the array II and the diagram of port distribution. The geometric dimensions of array II (unit: mm): $L_0 = 21.2$, $W_1 = 6$, $L_1 = 26.1$, $W_3 = 10.4$, $L_3 = 4$, $W_4 = 8.2$, $S_1 = 27.4$, $S_2 = 61$, $S_4 = 8.4$, $D = 34.9$ (0.44λ).
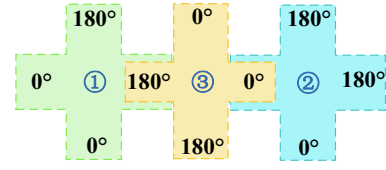

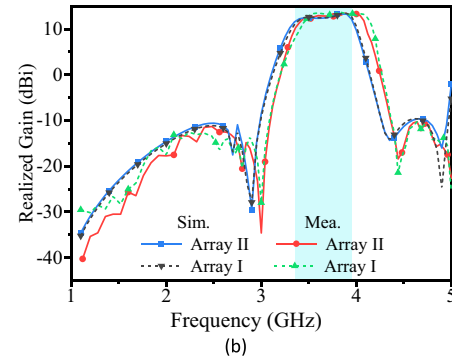**Fig. 27.** Scheme of feeding phases in array II.
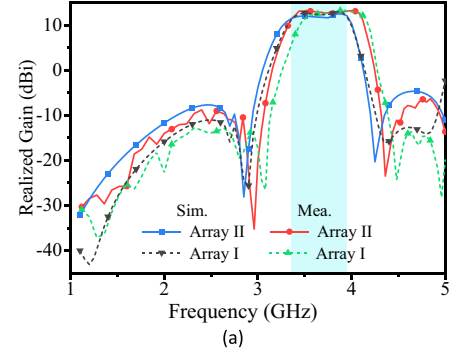
Fig. 28. Simulated and measured realized gains of the arrays I and II. (a) *x* polarization. (b) *y* polarization.
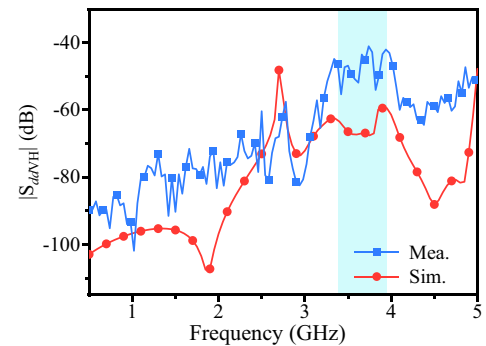
Fig. 29. Simulated and measured $|S_{ddVH}|$ of the array II.

3.3. Performance comparison

The proposed arrays I and II are compared with previously reported filtering antenna arrays in Table 1. It can be found from that the proposed array is highly integrated and has a low profile owing to the single layer substrate. Meanwhile, the novel array design results in a lower sidelobe level. Moreover, higher polarization isolations and better cross polarization ratios are achieved, with moderate gain and suppression levels. It is worthwhile noticing that an extra pair of the differential ports is used in the array II,

E-Plane   H-Plane

Fig. 30. Simulated and measured normalized radiation patterns in E-plane and H-plane of the array II at 3.65 GHz for *x* polarized feeding ports and *y* polarization feeding ports.

Fig. 31. Radiation pattern in H-plane of the arrays I and II at 3.65 GHz for *x* polarization. (a) Simulation. (b) Measurement.

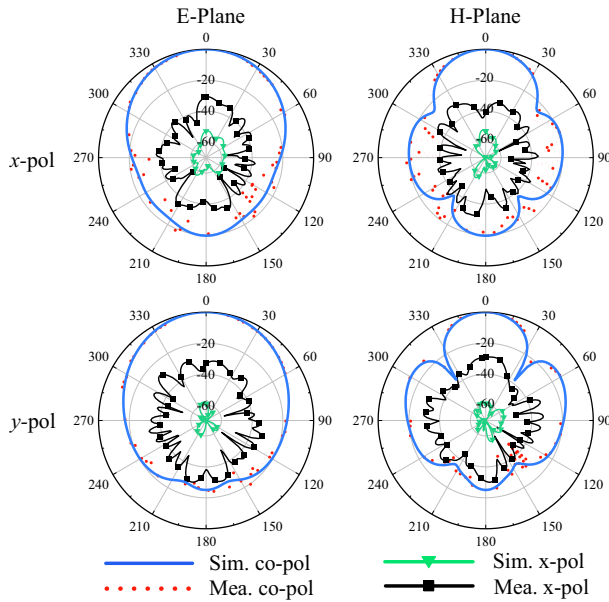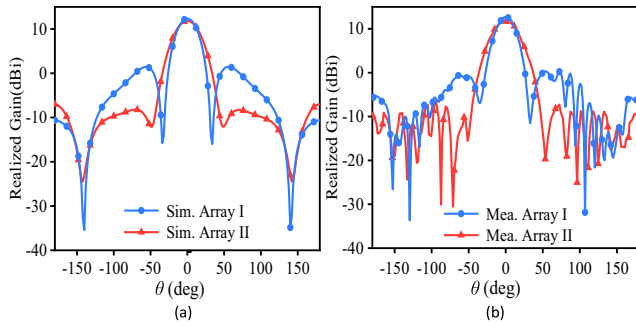compared with the array I. The use of the extra pair of the differential ports doesn't increase the overall size of the array II and the complexities of the feeding structure. Instead, better polarization isolation can be achieved. To sum up, the improved array has the better radiation performance while remaining the filtering response, compared with the conventional filtering antenna array.

4. Conclusions

In this paper, an integrated filtering antenna and its improved array has been presented. The single-layer dual-polarized filtering antenna element consisting of four driven patches and four radiation patches has two in-band resonances. The patches with the slots and the DGS are used to generate five controllable radiation nulls, and thus good out-of-band suppression is achieved. The prototype of the filtering antenna is fabricated, and the measured $|S_{dd21}|$ is -41 dB with the peak gain of 10.5 dBi. With the designed filtering antenna element, a novel array is developed by sharing the radiating patches. The designed array with the same size as the conventional 1×2 array has a smaller element spacing, thus resulting in the lower sidelobe level. The array prototype is fabricated and measured. The overall isolation related to two kinds of the polarized ports in the array itself is proposed, and the measured S_{ddVH} of the improved filtering antenna array is 41.1 dB. As a result, the proposed filtering array is of good radiation and filtering performance, which is good candidate for the base station MIMO array in 5G applications.

Declaration of Competing Interest

The authors declare that they have no known competing financial interests or personal relationships that could have appeared to influence the work reported in this paper.

Acknowledgments

Appendix

In this section, the isolation between two kinds of polarized ports in the multi-port differential network is derived. Consider a network diagram with 2*n* ports (*n* is even) shown in Fig. 32. In this network, 2*n* ports are successively called as $P_{1^+}, P_{1^-}, P_{2^+}, P_{2^-}, \cdots,$ P_{n^+}, P_{n^-}. Assume that the port P_{i^+} and P_{i^-} form a differential port D_i (*i* = 1, 2, 3, ..., *n*). In this scenario, there are *n* differential ports in this network. Without loss of generality, the differential ports $D_1, D_3, D_5, \ldots,$ and D_{n-1} excite *x* polarized wave, and the differential ports $D_2, D_4, D_6, \ldots,$ and D_n excite *y* polarized wave.

Without loss of generality, we denote S_{ddHV} and S_{ddVH} as the total isolation between two kinds of the polarized ports in the array. Here, the port *V* is composed of the all ports which excites *x* polarized wave, and the port *H* consists of the all ports which excite *y* polarized wave. From the input port *V* to the output port *H*, one has

Table 1
Performance comparison between reported dual-polarized filtering antenna arrays and proposed array.

	Element Spacing (λ_0)	Operation Band (GHz)/ Fractional Band (%)	Average Gain (dBi)/ Number of Elements	Cross-pol (dB)	PolarizationIsolation (dB)	SuppressionLevel (dB)	Sidelobe (dB)	Size (λ_0^3)
[2]	0.4	5.05–5.3/4.8	10/(2 × 2)	< −24	> 25*	> 19	–	1 × 1 × 0.063
	0.8	9.6–10.3/7	12/(2 × 2)	< −26	> 23*	> 14.5	−11	1.9 × 1.9 × 0.12
[5]	0.72	3.43–3.81/10.5	14/(1 × 4)	< −19	> 19*	> 9	−13	3.25 × 2.25 × 0.38
[8]	0.53	4.96–5.48/10	10.5/(2 × 2)	< −22	> 32*	> 17.5	−11	1.04 × 1.04 × 0.041
[13]	0.52	3.2–4.02/22.7	9.5/(1 × 3)	–	> 17*	> 20	−12	2.59 × 0.72 × 0.14
[21]	0.7	3.12–3.9/22.2	13.4/(1 × 4)	< −15	–	> 17.1	−12.5	2.81 × 0.7 × 0.15
[17]	0.54	24.25–29.5/19.5	11.2/(4 × 4)	< −20	> 30*	> 24	−13	3.13 × 3.13 × 0.16
Array I	**0.91**	**3.53–4.06/14**	**13.2/(1 × 2)**	**< −27**	**> 39.8**	**> 24.1**	**−12.36**	**2.07 × 1.22 × 0.038**
Array II	**0.44**		**13.1/improved (1 × 2)**	**< −26**	**> 41.1**	**> 19.7**	**−18.11**	

[a]The '*' in Table 1 means that the measured polarization isolation takes the effect of the power divider into account.
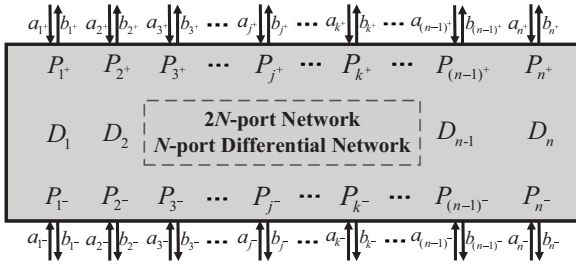
Fig. 32. $2n$-port network corresponding to n-port differential network schematic diagram.

$$a_i = \begin{cases} V^+/n, i = 1^+, 3^+, \cdots, (n-1)^+ \\ -V^+/n, i = 1^-, 3^-, \cdots, (n-1)^- \\ 0\ ,\ else \end{cases} \qquad (A\text{-}1)$$

Therefore, the S_{ddHV} can be solved as

$$S_{ddHV} = \frac{b_{2^+} - b_{2^-} + b_{4^+} - b_{4^-} + \cdots + b_{n^+} - b_{n^-}}{a_{1^+} - a_{1^-} + a_{3^+} - a_{3^-} + \cdots + a_{(n-1)^+} - a_{(n-1)^-}}$$

$$= \frac{1}{a_{1^+} - a_{1^-} + a_{3^+} - a_{3^-} + \cdots + a_{(n-1)^+} - a_{(n-1)^-}}.$$

$$[a_{1^+}(S_{2^+1^+} - S_{2^-1^+} + S_{4^+1^+} - S_{4^-1^+} + \cdots + S_{n^+1^+} - S_{n^-1^+})$$
$$+ a_{1^-}(S_{2^+1^-} - S_{2^-1^-} + S_{4^+1^-} - S_{4^-1^-} + \cdots + S_{n^+1^-} - S_{n^-1^-}) + \cdots$$
$$+ a_{n^+}(S_{2^+n^+} - S_{2^-n^+} + S_{4^+n^+} - S_{4^-n^+} + \cdots + S_{n^+n^+} - S_{n^-n^+})$$
$$+ a_{n^-}(S_{2^+n^-} - S_{2^-n^-} + S_{4^+n^-} - S_{4^-n^-} + \cdots + S_{n^+n^-} - S_{n^-n^-})]$$
$$= \frac{1}{n}[(S_{2^+1^+} - S_{2^-1^+} + S_{4^+1^+} - S_{4^-1^+} + \cdots + S_{n^+1^+} - S_{n^-1^+})$$
$$- (S_{2^+1^-} - S_{2^-1^-} + S_{4^+1^-} - S_{4^-1^-} + \cdots + S_{n^+1^-} - S_{n^-1^-}) + \cdots$$
$$+ (S_{2^+n^+} - S_{2^-n^+} + S_{4^+n^+} - S_{4^-n^+} + \cdots + S_{n^+n^+} - S_{n^-n^+})$$
$$- (S_{2^+n^-} - S_{2^-n^-} + S_{4^+n^-} - S_{4^-n^-} + \cdots + S_{n^+n^-} - S_{n^-n^-})]$$
$$(A\text{-}2)$$

Similarly, from the input port H to the output port V, S_{ddVH} can be expressed as

$$S_{ddVH} = \frac{1}{n}\Big[(S_{1^+2^+} - S_{1^-2^+} + S_{3^+2^+} - \cdots + S_{(n-1)^+2^+} - S_{(n-1)^-2^+})$$
$$- (S_{1^+2^-} - S_{1^-2^-} + S_{3^+2^-} - \cdots + S_{(n-1)^+2^-} - S_{(n-1)^-2^-}) + \cdots$$
$$+ (S_{1^+n^+} - S_{1^-n^+} + S_{3^+n^+} - \cdots + S_{(n-1)^+n^+} - S_{(n-1)^-n^+})$$
$$- (S_{1^+n^-} - S_{1^-n^-} + S_{3^+n^-} - \cdots + S_{(n-1)^+n^-} - S_{(n-1)^-n^-})\Big]$$
$$(A\text{-}3)$$

In the array II, some ports are reused, which is different from the conventional differential-fed arrays. As shown in Fig. 26, there are 6 differential ports, i.e., D_1, D_2, D_3, D_4, D_5 and D_6. The differential ports $D_1 \sim D_4$ are same as those of the array I. The D_5 is composed of port P_9 and P_{10}. Besides, the ports P_4 and P_6 also form a differential port D_6 for the reuse. The port V composed of the differential ports D_1, D_3 and D_5 excites x polarized wave, while the port H consisting of the differential ports D_2, D_4 and D_6 excites y polarized wave. In this scenario, we have

$$a_i = \begin{cases} V^+/4, i = 2, 6 \\ -V^+/4, i = 4, 8 \\ 0\ ,\ i = 1, 3, 5, 7, 9, 10 \end{cases} \qquad (A\text{-}4)$$

Furthermore, the S_{ddVH} can be obtained as

$$S_{ddVH} = \frac{b_1 - b_3 + b_5 - b_7 - b_9 + b_{10}}{a_2 - a_4 + a_6 - a_8}$$
$$= \frac{1}{4}[(S_{12} - S_{32} + S_{52} - S_{72} - S_{92} + S_{10\_2})$$
$$- (S_{14} - S_{34} + S_{54} - S_{74} - S_{94} + S_{10\_4})$$
$$+ (S_{16} - S_{36} + S_{56} - S_{76} - S_{96} + S_{10\_6})$$
$$- (S_{18} - S_{38} + S_{58} - S_{78} - S_{98} + S_{10\_8})]$$
$$(A\text{-}5)$$

References

[1] J. Qian, F. Chen, Y. Ding, H. Hu, Q. Chu, A wide stopband filtering patch antenna and its application in MIMO system, IEEE Trans. Antennas and Propag. 67 (1) (2019) 654–658.

[2] C.X. Mao, S. Gao, Y. Wang, Q. Luo, Q.X. Chu, A shared-aperture dual-band dual-polarized filtering-antenna-array with improved frequency response, IEEE Trans. Antennas Propag. 65 (4) (2017) 1836–1844.

[3] K.R. Xiang, F.C. Chen, Q. Tan, Q.X. Chu, High-selectivity filtering patch antennas based on multipath coupling structures, IEEE Trans. Microw. Theory Technol. 69 (4) (2021) 2201–2210.

[4] C. Lin, S. Chung, A filtering microstrip antenna array, IEEE Trans. Microw. Theory Technol. 59 (11) (2011) 2856–2863.

[5] C. Hua, R. Li, Y. Wang, Y. Lu, Dual-Polarized filtering antenna with printed Jerusalem-cross radiator, IEEE Access 6 (2018) 9000–9005.

[6] H. Hu, F. Chen, J. Qian, Q. Chu, A differential filtering microstrip antenna array with intrinsic common-mode rejection, IEEE Trans. Antennas Propag. 65 (12) (2017) 7361–7365.

[7] Z.H. Jiang, D.H. Werner, A compact, wideband circularly polarized co-designed filtering antenna and its application for wearable devices with low SAR, IEEE Trans. Antennas Propag. 63 (9) (2015) 3808–3818.

[8] C.X. Mao, S. Gao, Y. Wang, F. Qin, Q.X. Chu, Multimode resonator-fed dual-polarized antenna array with enhanced bandwidth and selectivity, IEEE Trans. Antennas Propag. 63 (12) (2015) 5492–5499.

[9] D.-S. La, J.-H. Zhao, S.-M. Chen, C.-X. Zhang, M.-J. Qu, J.-W. Guo, Dual-band omnidirectional coupled-fed monopolar filtering antenna, Int. J. Eng. Sci. Technol. 35 (2022) 101188.

[10] W.J. Yang, Y.M. Pan, X.Y. Zhang, A single-layer low-profile circularly polarized filtering patch antenna, IEEE Antennas Wirel. Propag. Lett. 20 (4) (2021) 602–606.

[11] J.F. Qian, F.C. Chen, Q.X. Chu, Q. Xue, M.J. Lancaster, A novel electric and magnetic gap-coupled broadband patch antenna with improved selectivity and its application in MIMO system, IEEE Trans. Antennas Propag. 66 (10) (2018) 5625–5629.

[12] Y.M. Pan, P.F. Hu, X.Y. Zhang, S.Y. Zheng, A low-profile high-gain and wideband filtering antenna with metasurface, IEEE Trans. Antennas Propag. 64 (5) (2016) 2010–2016.

[13] K. Xue, D. Yang, C. Guo, H. Zhai, H. Li, Y. Zeng, A dual-polarized filtering base-station antenna with compact size for 5G applications, IEEE Antennas Wirel. Propag. Lett. 19 (8) (2020) 1316–1320.

[14] Y. Li, Z. Zhao, Z. Tang, Y. Yin, Differentially-fed, dual-band dual-polarized filtering antenna with high selectivity for 5G sub-6 GHz base station applications, IEEE Trans. Antennas Propag. 68 (4) (2020) 3231–3236.

[15] J. Zeng, C. Wang, S. Zheng, X. Wang, A wideband filtering patch antenna array based on hybrid feeding scheme, in: 2019 International Symposium on Antennas and Propagation (ISAP) (2019).

[16] M. Li, S. Tian, M.C. Tang, L. Zhu, A compact low-profile hybrid-mode patch antenna with intrinsically combined self-decoupling and filtering properties, IEEE Trans. Antennas Propag. 70 (2) (2022) 1511–1516.

[17] Y. Zhang, W. Yang, Q. Xue, J. Huang, W. Che, Broadband dual-polarized differential-fed filtering antenna array for 5G millimeter-wave applications, IEEE Trans. Antennas Propag. 70 (3) (2022) 1989–1998.

[18] W. Yang, M. Xun, W. Che, W. Feng, Y. Zhang, Q. Xue, Novel compact high-gain differential-fed dual-polarized filtering patch antenna, IEEE Trans. Antennas Propag. 67 (12) (2019) 7261–7271.

[19] X. Zhang, Y. Zhang, Y. Pan, W. Duan, Low-Profile dual-band filtering patch antenna and its application to LTE MIMO system, IEEE Trans. Antennas Propag. 65 (1) (2017) 103–113.

[20] Y. Zhang, X. Zhang, L. Ye, Y. Pan, Dual-band base station array using filtering antenna elements for mutual coupling suppression, IEEE Trans. Antennas Propag. 64 (8) (2016) 3423–3430.

[21] Y. Li, Z. Zhao, Z. Tang, Y. Yin, Differentially-fed, wideband dual-polarized filtering antenna with novel feeding structure for 5G sub-6 GHz base station applications, IEEE Access 7 (2019) 184718–184725.

[22] J.A. Liu, Y.F. Cao, X.Y. Zhang, A pattern-reconfigurable filtering patch antenna using embedded resonators and switchable elements, IEEE Trans. Antennas Propag. 70 (5) (2022) 3828–3833.

[23] Q. Wu, Y. Shi, L. Li, P. Gas, Wideband dual-polarized differential-fed filtering microstrip patch antenna with high suppression and wide stopband, Int. J. RF Microw. Comput.-Aided Eng. 2023 (2023) 1–10.

[24] K. Li, Y. Shi, Filtering antenna synthesis based on characteristic mode theory, IEEE Trans. Antennas Propag. 70 (5) (2022) 3308–3319.

[25] D.M. Pozar, Microwave Engineering, 3nd ed., Wiley, New York, NY, USA, 1998, pp. 293–297.

[26] D. Ahn, J.S. Park, C.S. Kim, J. Kim, Y. Qian, T. Itoh, A design of the low-pass filter using the novel microstrip defected ground structure, IEEE Trans. Microw. Theory Technol. 49 (1) (2001) 86–93.